

## Article

# Tailoring Mesoporous Silicon Surface to Form a Versatile Template for Nanoparticle Deposition

Nadzeya Khinevich <sup>1,\*</sup>, Mindaugas Juodėnas <sup>1</sup>, Asta Tamulevičienė <sup>1,2</sup> , Hanna Bandarenka <sup>3,4</sup>   
and Sigitas Tamulevičius <sup>1,2,\*</sup> 

<sup>1</sup> Institute of Materials Science, Kaunas University of Technology, 59 K. Baršausko St., 51423 Kaunas, Lithuania; mindaugas.juodenas@ktu.lt (M.J.); asta.tamuleviciene@ktu.lt (A.T.)

<sup>2</sup> Department of Physics, Kaunas University of Technology, 50 Studentu St., 51368 Kaunas, Lithuania

<sup>3</sup> Applied Plasmonics Laboratory, Belarusian State University of Informatics and Radioelectronics, 6 Brovka St., 220013 Minsk, Belarus; h.bandarenka@bsuir.by

<sup>4</sup> The Polytechnic School, Ira A. Fulton Schools of Engineering, Arizona State University, 6075 S. Innovation Way West, Mesa, AZ 85212, USA

\* Correspondence: nadzeya.khinevich@ktu.edu (N.K.); sigitas.tamulevicius@ktu.lt (S.T.)

**Abstract:** Porous silicon (PS) can be used as a loading template in sensing or as a matrix to develop nanoparticle arrays. We present a comprehensive study of PS morphology and optical properties before and after the pore opening process, including the determination of thickness, pore size, and pore density of PS layers, its surface wettability, and reflectivity. The PS samples were fabricated by electrochemical anodization of monocrystalline silicon wafer in 5–20 wt.% hydrofluoric acid (HF) solution at a current density in the range of 20–200 mA/cm<sup>2</sup>. Anodization was followed by the pore opening process, i.e., the removal of a parasitic superficial layer with a “bottleneck” structure by reactive ion etching (RIE). The results illustrate that “bottleneck”-free PS allows to achieve a high pore density using a low HF concentration and a reduced current density. We established that this structure demonstrates higher hydrophobicity in comparison to the samples before RIE. The applicability of the developed “bottleneck”-free PS was tested via filling the pores with silver nanoparticles, indicating its potential use as a template for the fabrication of nanoparticle arrays.

**Keywords:** porous silicon; electrochemical etching; parasitic layer; reactive ion etching; nanoparticle array



**Citation:** Khinevich, N.; Juodėnas, M.; Tamulevičienė, A.; Bandarenka, H.; Tamulevičius, S. Tailoring Mesoporous Silicon Surface to Form a Versatile Template for Nanoparticle Deposition. *Coatings* **2021**, *11*, 699. <https://doi.org/10.3390/coatings11060699>

Academic Editor: Charafeddine Jama

Received: 10 May 2021

Accepted: 8 June 2021

Published: 10 June 2021

**Publisher's Note:** MDPI stays neutral with regard to jurisdictional claims in published maps and institutional affiliations.



**Copyright:** © 2021 by the authors. Licensee MDPI, Basel, Switzerland. This article is an open access article distributed under the terms and conditions of the Creative Commons Attribution (CC BY) license (<https://creativecommons.org/licenses/by/4.0/>).

## 1. Introduction

Porous silicon (PS) represents an intriguing platform to engineer miniature sensors compatible with Si technology that provide accurate and reliable detection of various organic molecules in a liquid or gaseous environment. The unique structural and optical properties of this porous material are easily tuned via the variation of regimes of its formation during the electrochemical anodization of monocrystalline silicon, which is the most convenient and affordable method to be used in both a research laboratory and industrial facilities [1,2].

The anodization of silicon wafers is usually accompanied by the growth of a thin parasitic layer caused by surface defects (e.g., surface roughness or uneven distribution of doping atoms) on the initial monocrystalline substrate. This surface layer usually consists of pores with a lower diameter compared to the pores distributed in the deeper layer, resulting in the so-called “bottleneck” effect. Therefore, it can strongly affect the morphology, mechanical, and electrical properties of the final PS-based device [3]. Such an effect is critical for the mesoporous silicon used to host or to capture nanostructures of other materials. Many applications imply the full filling of mesopores, which cannot be achieved due to the presence of the “bottleneck” layer [4]. For instance, mesoporous silicon is a suitable material for sensing elements because the pore diameters are equal or easily

adjustable to the size of organic molecules of the analyzed media. However, the parasitic layer can hamper their incorporation and diffusion within the porous matrix. Therefore, there is a need for the removal of the parasitic layer or prevention of its occurrence to provide a high loading effect of the PS sensing components [5]. Various methods to achieve this objective through the destruction of the “bottleneck” are reported. Among them, such methods as chemical dissolution [6,7], oxidation of PS followed by silicon dioxide removal in hydrofluoric acid (HF) [8], electropolishing, and plasma etching [9] have been demonstrated. Plasma etching is characterized by several advantages in comparison to other techniques [9]. The structural, chemical, electrical, and optical properties of the PS samples not subjected to the “bottleneck” layer removal have been thoroughly characterized and reported in [2,10,11]. However, the features of the final porous material free of the parasitic layer have not been sufficiently studied, despite their strong influence on the efficiency and reliability of the final devices containing PS components.

In the present work, PS was fabricated by electrochemical anodization at different formation conditions (HF concentration in the electrolyte and current density), and the parasitic layer was removed by reactive ion etching (RIE).

We present a comprehensive study of PS morphology and optical properties before and after the pore opening process provided via the removal of the parasitic layer. This work included the determination of the thickness, pore size, and pore density of the PS layers, its surface wettability, and reflectivity. The reflectance spectra of the PS layers were used to calculate the average refractive index. The influence of the HF concentration in the electrolyte and current density on the original size of pores was studied to define optimal conditions to produce nanostructures that can be used as templates for metal nanoparticles' (NPs) deposition.

## 2. Materials and Methods

Antimony-doped Si (100) wafer (Siegert Wafer, Aachen, Germany) with the resistivity of 0.008–0.02 ohm·cm was used for the PS formation. Before etching, the native silicon dioxide was removed in a low concentration (4 wt.%) hydrofluoric acid (Fluka, Seezle, Germany) solution. The electrochemical etching for the PS formation was carried out in an aqueous HF solution at different concentrations (5, 10, and 20 wt.%) for 90 s. Current density ( $j$ ) was varied from 20 mA/cm<sup>2</sup> to 200 mA/cm<sup>2</sup>. The removal of the parasitic surface layer was performed using RIE for 5 min in a 50 sccm gas flow of SF<sub>6</sub> at 20 mT pressure, 40 V bias voltage, and 500 W ICP (inductively coupled plasma) coil power (Vision LL-ICP, Plasma-Therm, Lomma, Sweden). After the RIE process, all the PS samples were cleaned in an ultrasonic bath in chloroform for 5 min to remove the oil that was used to bond them to a carrier wafer. Just before the characterization, the PS layers were treated with the diluted HF solution for a few seconds to remove oxidized areas.

The morphology and thickness of the PS samples were investigated using a scanning electron microscope FEI Quanta 200 FEG (FEI, Hillsboro, OR, USA) and analyzed using ImageJ software [12]. A drop shape analyzer DSA 25 (Kruss GmbH, Hamburg, Germany) was used for determining the water contact angle of the samples. The sessile drop method was applied for the contact angle determination.

Optical reflectance spectra of the PS layers were collected in the 400–800 nm spectral range with an optical microscope Olympus equipped with a fiber-optic spectrometer AvaSpec-2048 (Avantes, Apeldoorn, Netherlands) with 1.4 nm resolution.

To check the possibility to use PS as a template for the metal nanoparticles' deposition, spherical silver nanoparticles of 62 nm diameter with ~10% standard deviation in size were synthesized according to a previously described method [13]. In brief, the procedure of nanoparticles' synthesis consisted of two typical steps. At first, 100 mL of seed solution was prepared using 0.05 mM of tannic acid (TA) (Sigma-Aldrich, China), 5 mM of trisodium citrate (TC) (Lach-Ner, Neratovice, Czech Republic) and 0.025 mM silver nitrate (AgNO<sub>3</sub>) (Girochem, Teplička nad Váhom, Slovenia) in Milli-Q water (Merck, Massachusetts, USA). Afterwards, the particles' size was tuned in the second synthesis step-growth of the seeds.

For this procedure 19.5 mL of seed solution was mixed with 16.5 mL of water and heated under the 90 °C. Then 500 mL of TC (25 mM), 1.5 mL of TA (2.5 mM) and 1 mL of AgNO<sub>3</sub> (25 mM) were added and kept heated and stirred for 30 min. The second step was repeated three times until the required nanoparticles' size was achieved. Synthesized silver NPs were deposited on PS by a capillary-assisted particle assembly (CAPA) procedure [14,15].

### 3. Results and Discussion

#### 3.1. Surface Morphology

Scanning electron microscopy (SEM) top views and the pore diameter distribution of the standard, pre-polished, and RIE-treated PS samples are shown in Figure 1. The “standard” PS was fabricated using 10 wt.% HF solution at 100 mA/cm<sup>2</sup>, whereas the “pre-polished” PS sample was additionally subjected to primary surface electropolishing at a current density of 3 A/cm<sup>2</sup> for 1 min.

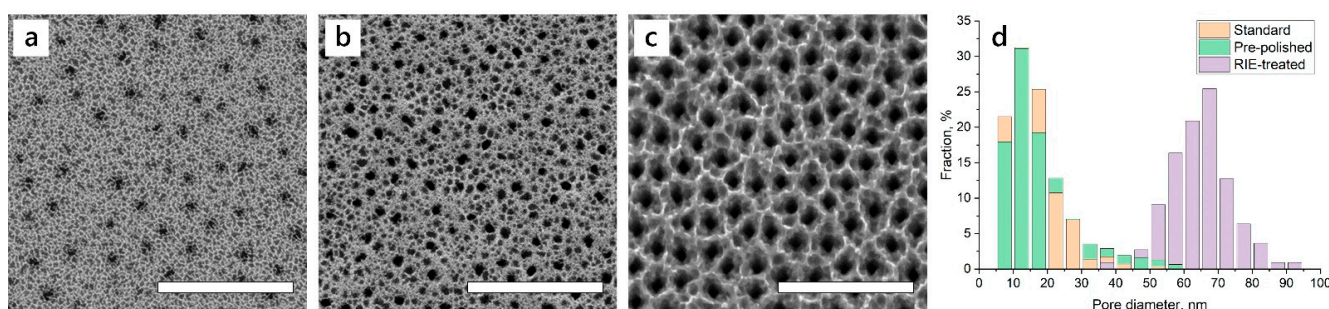


**Figure 1.** Scanning electron microscopy (SEM) top views of porous silicon (PS) formed in 10 wt.% hydrofluoric acid (HF) solution at 100 mA/cm<sup>2</sup> current density: (a) standard, (b) pre-polished, and (c) standard after reactive ion etching (RIE). The scale bar is 500 nm. (d) Pore size (diameter) distribution of the corresponding samples.

According to the SEM top-view images of the PS surface, one can see that the single-step electrochemical anodization process produces at least two different layers. The first layer is composed of small pores with a diameter of 15–20 nm that are irregularly shaped and randomly arranged. These pores are separated by silicon walls of the nanoscaled thickness (Figure 1a). A similar layer is observed on the pre-polished sample (Figure 1b). This layer has nearly the same surface morphology, but the size distribution of pore diameters becomes broader, and the number of “black” pores increases in comparison to the standard PS sample morphology (Figure 1a). It seems that the polishing procedure before the electrochemical anodization minimizes the number of defects on the surface, but some of them are still present and contribute to further PS formation. The pore size distribution determined for the sample after RIE (Figure 1c) indicates that the parasitic “bottleneck” layer was removed and the second layer with a mean pore size of 60–70 nm was uncovered (Figure 1d).

Figure 2 shows the SEM images of one set of the PS samples before and after RIE, formed at  $j = 60$  mA/cm<sup>2</sup> in 5 wt.%, 10 wt.%, and 20 wt.% HF solutions. The morphology of the RIE-treated PS formed in the electrolyte with 5 wt.% (for all samples) and 10 wt.% HF (at high current density) mostly looks smooth, and only a slight increase in the roughness of the PS indicates isotropic etching of the top layer. The surface of the samples made at 10 wt.% HF at a low current density (20–60 mA/cm<sup>2</sup>) and for all samples made in 20 wt.% HF is characterized by the formation of a porous layer, which consists of islands that make the surface rough. These substrates seem to be much less sensitive to liquid substances or nanoparticles loading into PS than the others with higher pore density.

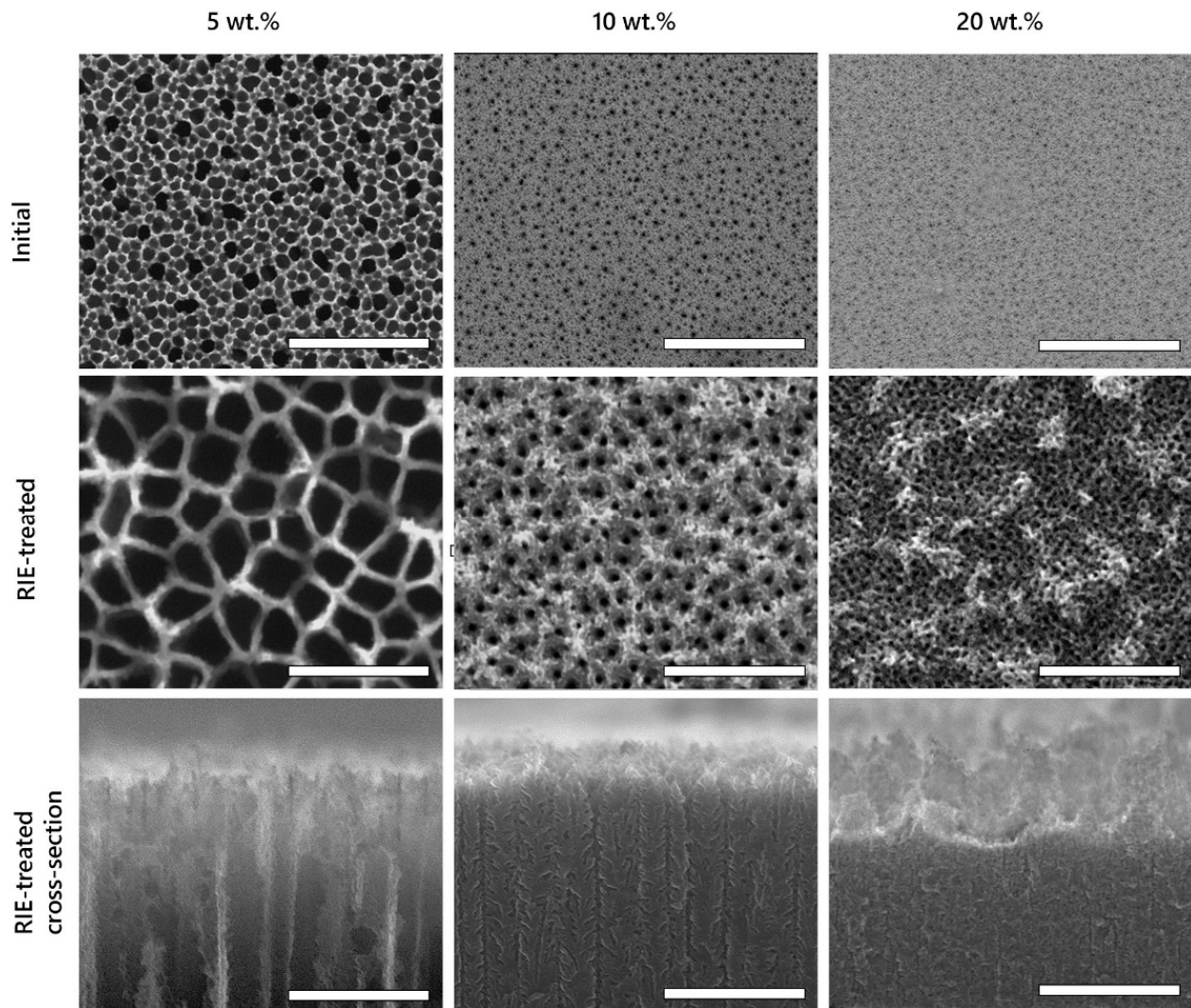


**Figure 2.** Top view of initial PS (on top) formed at  $j = 60 \text{ mA/cm}^2$  in the electrolyte with HF concentration 5 wt.%, 10 wt.%, 20 wt.%. Top view and cross-section of the same samples after RIE treatment (at the bottom). The scale bar is 500 nm.

In addition, these results demonstrate that RIE is a suitable method to remove the surface layer without damaging the inner morphology of the formed PS layers (Figure 2).

In general, the pores look uniform throughout the analyzed areas. The mean pore diameter and the density of the pores are presented in Figure 3. One can see that the mean diameter increases with the rise of current density. This linear dependence is followed until some critical value of current density is reached and the pore size starts to decrease. It should be noted that the critical current density value depends on the HF concentration, i.e., for 5 wt.% HF solution, the maximum pore diameter of  $\sim 130 \text{ nm}$  is reached at  $60 \text{ mA/cm}^2$ , whereas for 10 wt.% HF solution a  $160 \text{ nm}$  pore diameter is observed at  $140 \text{ mA/cm}^2$ . These regularities can be explained by changes in the mechanism of PS formation by anodization [16]. At high current densities, the produced pores become spatially irregular, and a sponge-like structure is formed. The Si skeleton becomes thinner, and the pore density increases. Further increase in the current density leads to the electropolishing process. Moreover, the electropolishing can be predicted by the pore density value, e.g., we have experimentally confirmed that in 5 wt.% HF solution this process starts at  $100 \text{ mA/cm}^2$ , and for 10 wt.% HF, current density must be higher than  $400 \text{ mA/cm}^2$ .

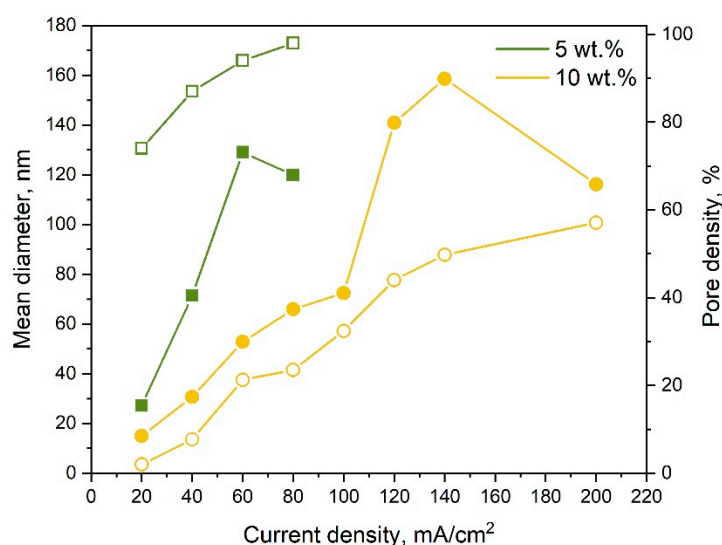


**Figure 3.** Dependence of the mean diameter (filled symbols) and pore density (empty symbols) on the applied current density of the PS samples formed at different HF concentrations.

The PS thickness growth rate was determined from the cross-section analysis of SEM images. It was established that the rate of the layer thickening is in direct dependence on the applied current density. At the same time, we can observe that thicker layers were created at higher HF concentrations during the same process time (Figure 4). The analysis of the thickness of the RIE-treated PS layers shows that the RIE process runs slower for PS with lower pore density. The RIE speed sharply increases for the samples fabricated in 5 wt.% HF at  $j = 80 \text{ mA/cm}^2$  due to the high density of pores (which reaches up to 96%) and thin Si walls. After the RIE, we observed that the most moiety of the PS layer was removed and the thickness of the produced structure was about 500 nm, whereas the initial thickness was about 2.6  $\mu\text{m}$ .

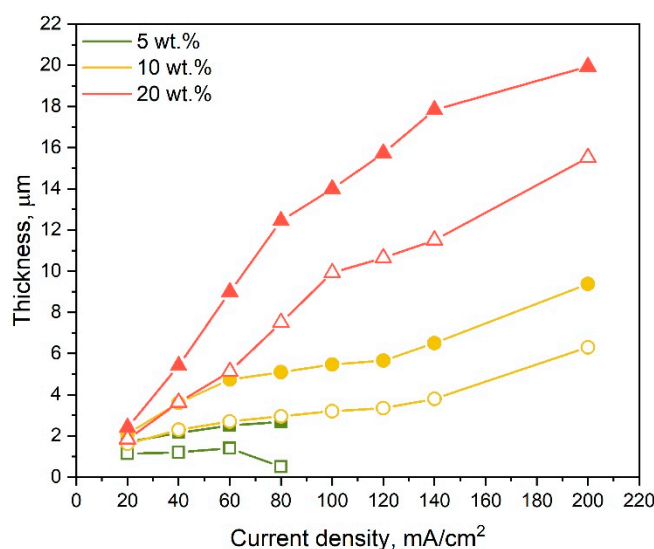


**Figure 4.** The PS thickness dependence on applied current density during electrochemical anodization in different concentration HF solutions. Initial PS samples are marked with filled symbols, RIE-treated samples with unfilled symbols.

### 3.2. Surface Wettability

The surface wettability is an essential surface characteristic in the case when the PS is designed to be used as a component of a sensor. Figure 5 shows that the PS hydropho-

bicity is much higher than that of the monocrystalline Si, for which the contact angle was measured to be  $91^\circ$  (Figure 5b).

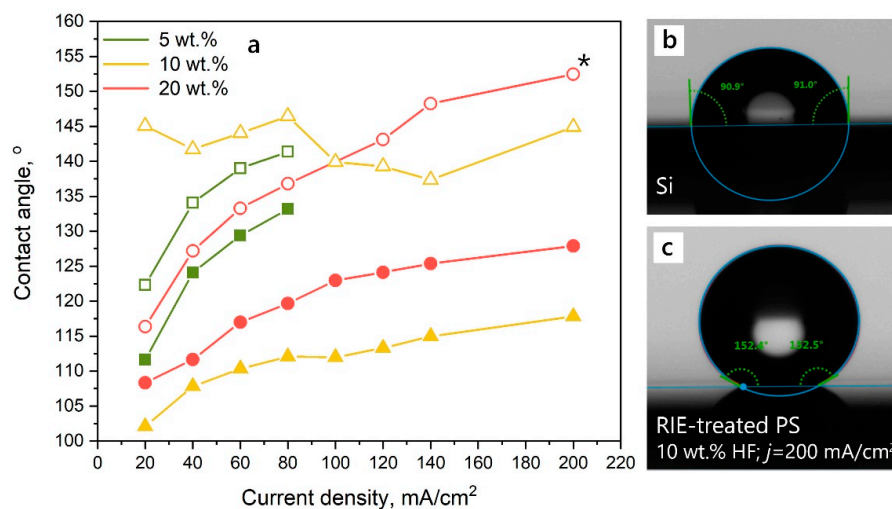


**Figure 5.** The contact angle of the PS samples before and after RIE. (a) the dependence of water contact angle on the current density applied during the anodization process of porous silicon. Initial PS samples are marked with filled symbols, RIE-treated samples with unfilled symbols; (b) water contact angle measured on bare Si and (c) on RIE-treated PS formed in 10 wt.% HF solution at  $j = 200 \text{ mA/cm}^2$  (contact angle value is indicated with the “\*” mark in the graph).

The contact angle of the standard PS samples looks to be smaller than the contact angle of RIE-treated samples, but it shows the same behavior in dependence on the current density, i.e., the PS hydrophobicity increases with the increase of current density. The contact angle value changed from  $112^\circ$  to  $133^\circ$ , from  $108^\circ$  to  $127^\circ$ , and from  $102^\circ$  to  $118^\circ$  for the PS samples formed in 5 wt.%, 10 wt.%, and 20 wt.% HF solutions, respectively. The contact angle of the RIE-treated PS samples formed in 5 wt.% and 10 wt.% HF solution increased from  $122^\circ$  to  $141^\circ$ , and from  $116^\circ$  to  $152^\circ$  respectively (Figure 5a). In the final case, the PS layer formed in 10 wt.% HF and at  $j = 200 \text{ mA/cm}^2$  (marked in the graph) demonstrates the superhydrophobic effect as the contact angle is greater than  $150^\circ$  (Figure 5c).

In the case of the RIE-treated PS substrate formed in 20 wt.% HF solution, no clear dependence of the contact angle on the current density was observed. Such an effect is interplayed with the rough surface morphology that was found to be almost independent on the applied current density.

The results illustrate that in all the cases when the PS was produced using the HF concentrations lower than 20 wt. %, the contact angle (or wettability of the surface) can be easily adjusted using different current densities applied in a course of the anodization. Moreover, RIE contributes to an additional increase in the contact angle.

To successfully use the PS as a template for nanoparticles' assembly by CAPA, the contact angle of a suspension of nanoparticles and the substrate must be properly tuned to achieve a high assembly yield. According to several studies [17–19], the value of the contact angle ensuring a successful assembly is in the range from  $30^\circ$  to  $75^\circ$ . In the PS case, such conditions can be set by reducing the free surface energy using surfactants [20] or changing the template wetting behavior by oxidation [21], oxygen plasma treatment [22], or functionalization [23].

### 3.3. Optical Properties

Optical characterization of the PS layers, especially the investigation of the refractive index, is the most important task for further development of photonic sensors based on this porous material [24]. It is known that the PS surface layer consists of silicon crystallites and pores that contribute to diffuse scattering and final reflectivity.

The measured PS reflectance spectra (for samples formed at 5 wt.% and 10 wt.% HF) show a series of interference fringes that correspond to the constructive and destructive interference of the reflected light from air/PS and PS/Si interfaces that are also called Fabry–Pérot interference fringes (Figure 6). Using the Fabry–Pérot interference principle [25], the effective optical thickness (EOT)  $2n_{PS}L$  was evaluated and then the value of the average refractive index ( $n_{PS}$ ) was extracted from EOT using the value of PS layer thickness ( $L$  values were taken from Figure 4). The results obtained are presented in Table 1. The frequency of the interference fringes strongly depends on the air fraction values in the PS structure [26].

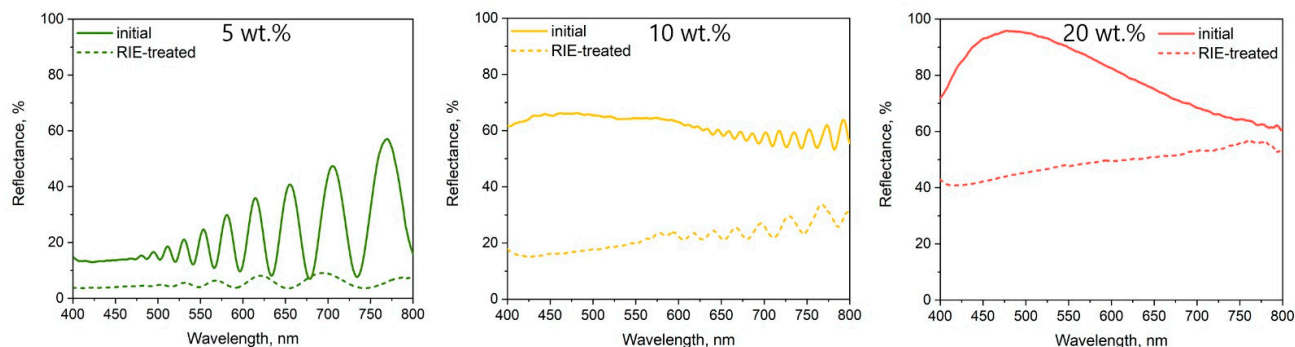


**Figure 6.** Reflectance spectra of initial PS (solid line) and RIE-treated (dashed line) formed at  $j = 60 \text{ mA/cm}^2$  in the electrolyte with HF concentration of 5 wt.%, 10 wt.%, 20 wt.%.

**Table 1.** The Average Refractive Index of Initial and RIE-treated PS.

HF Conc.		Current Density ( $\text{mA/cm}^2$ )							
		20	40	60	80	100	120	140	200
5 wt.%	initial	3.21	2.48	1.39	1.20	-	-	-	-
	RIE-treated	3.35	2.50	1.41	1.57	-	-	-	-
10 wt.%	initial	3.24	3.14	2.99	2.73	2.40	2.13	2.10	2.01
	RIE-treated	-	3.17	2.97	2.87	2.72	2.20	2.17	2.04

The refractive index was calculated for the samples made using 5 wt.% and 10 wt.% HF electrolytes. According to Table 1, the refractive index decreases with the increase of the applied current density, and this is usually related to the increase of pore density (porosity) [27]. The exception is observed for the PS sample formed in 5 wt.% at  $j = 80 \text{ mA/cm}^2$ , where the refractive index increases sharply. We attribute this to the contribution of Si to the reflection spectra due to the small amount of the remaining PS after etching (see Section 3.1). In general, the RIE-treated samples are regarded as a single-layer structure, whereas the initial samples are considered to be multi-layer consisting of the layers with different porosity. In most cases, the refractive index value of the initial PS samples is slightly lower than that of RIE-treated samples. This can be explained by the presence of a highly porous surface parasitic layer that contributes to the refractive index and decreases its value. Only in a single case (10 wt.% HF;  $j = 60 \text{ mA/cm}^2$ ), the refractive index of the RIE-treated PS sample is smaller than the value of the initial PS sample, but the difference is rather small, and it could be attributed to the thickness estimation errors.

The reflectance spectra of the initial PS samples prepared in 20 wt.% HF solution (Figure 6) look similar to the spectrum of the bare silicon. We assume that the porosity of these samples is so low that we cannot observe any major changes in their optical properties. The RIE-treated PS reflectivity is characterized by a lower intensity due to the scattering effect that occurs on a rough surface. In both cases, the reflectance spectra demonstrate fringes with a very low amplitude that are hardly distinguished and cannot be used for

further determination of optical parameters. The optical parameters were not determined for the sample formed in 10 wt.% HF and  $j = 20 \text{ mA/cm}^2$  due to the same difficulties.

### 3.4. Reactive Ion Etching (RIE) Etched Porous Silicon Templates for the Nanoparticles' Deposition

The “bottleneck”-free PS substrate has great potential as a template, which provides a precise definition of shape, size, and spatial location of different nanostructures for the development of radically new metamaterials with outstanding magnetic, optical, catalytic, and other features. As a proof of concept of this work, we demonstrated how the mesoporous silicon with pores opened by the RIE treatment can be used for ordered embedding of spherical silver nanoparticles possessing the prominent surface plasmon resonance (SPR) in the blue range of the optical spectrum. In particular, this property is in high demand to design and engineer components of Si-based devices for photovoltaic and sensing applications.

In our work, we deposited silver nanoparticles on the PS samples made in 10 wt.% HF solution and at  $j = 100 \text{ mA/cm}^2$ . Silver nanoparticles with a mean diameter of 62 nm with  $\sim 10\%$  standard deviation in size were used. The diameter of the spherical silver nanoparticles was selected in accordance to the pore size of the developed PS sample and based on the research showing the successful use of such particles' size in sensing experiments [28]. The CAPA method [14] was selected for the silver nanoparticles' deposition. Namely this approach provides the most controlled distribution of the colloidal nanoparticles over a template's surface compared to other techniques (e.g., drop deposition). The PS surface after the silver nanoparticles' deposition is shown in Figure 7 (the top view of the RIE-treated PS sample before NPs implementation is presented in Figure 1c). To show the importance of surface morphology on the deposition yield the particles were applied on the initial sample and on RIE-treated sample in the same conditions (Figure 7). In both cases similar silver nanoparticles were used. The PS sample not subjected to the RIE treatment provided anchoring of the silver nanostructures in some places around the sample surface but their distribution was uneven (Figure 7a). Due to a mismatch of pore and silver nanoparticle diameter, all the particles were distributed on the top of the surface. On the other hand, when the surface layer was etched away, the silver nanoparticles penetrated nearly all the pores (pore entrance filling factor was  $\sim 85\%$ ). It should be noted that in rare cases, a few nanoparticles occupied one pore or were displaced to the edge of the pore. It should be highlighted that the removal of the “bottleneck” layer led to opening the structure that provided deposition of the highly ordered ensemble of the silver nanoparticles divided by the silicon walls of the nano scaled thickness. The final structure had the prospect of possessing an extremely intensive electromagnetic field in the spots of silver nanoparticle and silicon wall contact, due to plasmonic coupling between metallic nanoparticles and semiconductor [29]. What is also important, the distance between the nanoparticles can be tuned as well as the pore size and particle diameter by varying anodization and synthesis conditions, respectively.

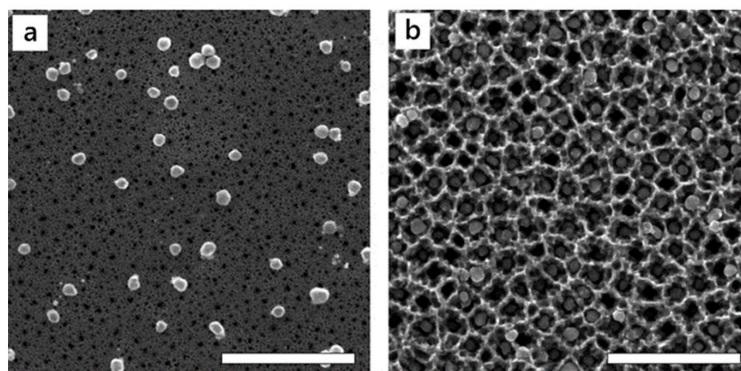


**Figure 7.** Top view of the initial (a) and the RIE-etched PS (b) made in 10 wt.% HF solution and at  $j = 100 \text{ mA/cm}^2$  after Ag nanoparticles deposition. The scale bar is 500 nm.

#### 4. Conclusions

We demonstrated that RIE is an efficient method for the removal of the parasitic surface layer without damaging the morphology of the PS. The analysis of the electrochemical anodization conditions revealed that the properties of the PS (pore size and density, refractive index, wettability) can be tuned in a wide range. Changing the current density and HF concentration during the electrochemical etching process enables the pore size to be managed in a range from 10 nm up to 160 nm. We showed that the surface wettability is in a good dependence on current density and by selecting proper conditions we can create hydrophobic ( $100^\circ$ ) or superhydrophobic ( $152^\circ$ ) structures. The optimal HF concentration for the creation of porous structures was determined to be in the range of 5–10 wt.%, whereas PS formed at 20 wt.% HF concentration comprised of islands that reduce the flatness of the surface. The RIE-etched PS sample formed at 10 wt.% HF solution was shown to be a favorable template for the CAPA deposition of the highly ordered array of the 62 nm size silver nanoparticles divided by silicon walls with the filling factor of ~85%, which are expected to possess prominent plasmonic properties and present the object of a future study. The selection of the described electrochemical etching conditions allows us to create templates with a variable pore size and to adapt the surface morphology to nanoparticle deposition.

**Author Contributions:** Conceptualization, N.K., A.T., S.T. and H.B.; methodology, N.K. and M.J.; investigation, N.K.; resources, N.K., A.T.; writing—original draft preparation, N.K., A.T. and H.B.; writing—review and editing, all authors. All authors have read and agreed to the published version of the manuscript.

**Funding:** N.K: M.J, A.T., and S.T. acknowledge funding from the Research Council of Lithuania (LMTLT) (Agreement No.P-LZ-21-1).

**Institutional Review Board Statement:** Not applicable.

**Informed Consent Statement:** Not applicable.

**Data Availability Statement:** Not applicable.

**Conflicts of Interest:** The authors declare no conflict of interest.

#### References

1. Jane, A.; Dronov, R.; Hodges, A.; Voelcker, N.H. Porous silicon biosensors on the advance. *Trends Biotechnol.* **2009**, *27*, 230–239. [[CrossRef](#)]
2. Canham, L. *Handbook of Porous Silicon*; Springer International Publishing: Berlin, Germany, 2018; Volume 1–2, ISBN 9783319713816.
3. Redko, S.V.; Bondarenko, V.P.; Petrovich, V.A.; Kotov, D.A.; Chubenko, E.B.; Sherstnyov, A.I. Influence of the Surface Layer on the Electrochemical Deposition of Metals and Semiconductors into Mesoporous Silicon. *Semiconductors* **2016**, *50*, 372–376. [[CrossRef](#)]
4. Mariani, S.; Pino, L.; Strambini, L.M.; Tedeschi, L.; Barillaro, G. 10 000-Fold Improvement in Protein Detection Using Nanostructured Porous Silicon Interferometric Aptasensors. *ACS Sens.* **2016**, *1*, 1471–1479. [[CrossRef](#)]
5. Mariani, S.; Strambini, L.M.; Barillaro, G. Electrical Double Layer-Induced Ion Surface Accumulation for Ultrasensitive Refractive Index Sensing with Nanostructured Porous Silicon Interferometers. *ACS Sens.* **2018**, *3*, 595–605. [[CrossRef](#)]
6. Chamard, V.; Dolino, G.; Muller, F. Origin of a parasitic surface film on p+ type porous silicon. *J. Appl. Phys.* **1998**, *84*, 6659–6666. [[CrossRef](#)]
7. Harraz, F.A.; El-Sheikh, S.M.; Sakka, T.; Ogata, Y.H. Cylindrical pore arrays in silicon with intermediate nano-sizes: A template for nanofabrication and multilayer applications. *Electrochim. Acta* **2008**, *53*, 6444–6451. [[CrossRef](#)]
8. Sciacca, B.; Secret, E.; Pace, S.; Gonzalez, P.; Geobaldo, F.; Quignard, F.; Cunin, F. Chitosan-functionalized porous silicon optical transducer for the detection of carboxylic acid-containing drugs in water. *J. Mater. Chem.* **2011**, *21*, 2294–2302. [[CrossRef](#)]
9. Errien, N.; Vellutini, L.; Louarn, G.; Froyer, G. Surface characterization of porous silicon after pore opening processes inducing chemical modifications. *Appl. Surf. Sci.* **2007**, *253*, 7265–7271. [[CrossRef](#)]
10. Korotcenkov, G. *Porous Silicon: From Formation to Application: Formation and Properties, Volume One*; Korotcenkov, G., Ed.; CRC Press: Boca Raton, FL, USA, 2016; ISBN 9780429076503.
11. Torres-Costa, V.; Martín-Palma, R.J. Application of nanostructured porous silicon in the field of optics. A review. *J. Mater. Sci.* **2010**, *45*, 2823–2838. [[CrossRef](#)]
12. ImageJ Software. Available online: <https://imagej.nih.gov/ij/index.html> (accessed on 4 June 2021).
13. Bastús, N.G.; Merkoçi, F.; Piella, J.; Puentes, V. Synthesis of highly monodisperse citrate-stabilized silver nanoparticles of up to 200 nm: Kinetic control and catalytic properties. *Chem. Mater.* **2014**, *26*, 2836–2846. [[CrossRef](#)]

14. Juodenas, M.; Tamulevičius, T.; Henzie, J.; Erts, D.; Tamulevičius, S. Surface Lattice Resonances in Self-Assembled Arrays of Monodisperse Ag Cuboctahedra. *ACS Nano* **2019**, *13*, 9038–9047. [[CrossRef](#)]
15. Juodenas, M.; Peckus, D.; Tamulevičius, T.; Yamauchi, Y.; Tamulevičius, S.; Henzie, J. Effect of Ag Nanocube Optomechanical Modes on Plasmonic Surface Lattice Resonances. *ACS Photonics* **2020**. [[CrossRef](#)]
16. Zhao, M.; McCormack, A.; Keswani, M. The formation mechanism of gradient porous Si in a contactless electrochemical process. *J. Mater. Chem. C* **2016**, *4*, 4204–4210. [[CrossRef](#)]
17. Ni, S.; Isa, L.; Wolf, H. Capillary assembly as a tool for the heterogeneous integration of micro- and nanoscale objects. *Soft Matter* **2018**, *14*, 2978–2995. [[CrossRef](#)]
18. Malaquin, L.; Kraus, T.; Schmid, H.; Delamarche, E.; Wolf, H. Controlled particle placement through convective and capillary assembly. *Langmuir* **2007**, *23*, 11513–11521. [[CrossRef](#)]
19. Kang, J.; Park, C.G.; Lee, S.H.; Cho, C.; Choi, D.G.; Lee, J.Y. Fabrication of high aspect ratio nanogrid transparent electrodes: Via capillary assembly of Ag nanoparticles. *Nanoscale* **2016**, *8*, 11217–11223. [[CrossRef](#)]
20. Spencer, S.J.; Andrews, G.T.; Deacon, C.G. Contact angle of ethanol-water solutions on crystalline and mesoporous silicon. *Semicond. Sci. Technol.* **2013**, *28*. [[CrossRef](#)]
21. Muñoz, E.C.; Díaz, C.; Navarrete, E.; Henríquez, R.; Schrebler, R.; Córdova, R.; Marotti, R.; Heyser, C. Characterization of surface changes on silicon and porous silicon after interaction with hydroxyl radicals. *Arab. J. Chem.* **2019**, *12*, 5125–5133. [[CrossRef](#)]
22. Jiang, L.; Li, S.; Wang, J.; Yang, L.; Sun, Q.; Li, Z. Surface wettability of oxygen plasma treated porous silicon. *J. Nanomater.* **2014**, *2014*. [[CrossRef](#)]
23. Dattilo, D.; Armelao, L.; Maggini, M.; Fois, G.; Mistura, G. Wetting behavior of porous silicon surfaces functionalized with a fulleropyrrolidine. *Langmuir* **2006**, *22*, 8764–8769. [[CrossRef](#)]
24. Lammel, G.; Schweizer, S.; Schiesser, S.; Renaud, P. Tunable optical filter of porous silicon as key component for a MEMS spectrometer. *J. Microelectromech. Syst.* **2002**, *11*, 815–828. [[CrossRef](#)]
25. Paes, T.F.; Beloto, A.F.; Galvão, E.C.D.S.; Berni, L.A. Simple method for measuring the porosity, thickness and refractive index of porous silicon, based on the Fabry-Pérot interference spectrum. *Rev. Bras. Apl. Vácuo* **2017**, *35*, 117. [[CrossRef](#)]
26. Maniya, N.H.; Patel, S.R.; Murthy, Z.V.P. Electrochemical preparation of microstructured porous silicon layers for drug delivery applications. *Superlattices Microstruct.* **2013**, *55*, 144–150. [[CrossRef](#)]
27. Sohn, H. Refractive Index of Porous Silicon. In *Handbook of Porous Silicon*; Canham, L., Ed.; Springer: Cham, Switzerland, 2018; pp. 241–352. [[CrossRef](#)]
28. Stamplecoskie, K.G.; Scaiano, J.C.; Tiwari, V.S.; Anis, H. Optimal size of silver nanoparticles for surface-enhanced raman spectroscopy. *J. Phys. Chem. C* **2011**, *115*, 1403–1409. [[CrossRef](#)]
29. Casadei, A.; Pecora, E.F.; Trevino, J.; Forestiere, C.; Rüffer, D.; Russo-Averchi, E.; Matteini, F.; Tutuncuoglu, G.; Heiss, M.; Fontcuberta I Morral, A.; et al. Photonic-plasmonic coupling of GaAs single nanowires to optical nanoantennas. *Nano Lett.* **2014**, *14*, 2271–2278. [[CrossRef](#)] [[PubMed](#)]